Subcellular context-specific tuning of actomyosin ring contractility within a common cytoplasm

John B. Linehan[1], Alexandra Zampetaki[2], Michael E. Werner[1], Bryan Heck[1], Paul S. Maddox[1], Sebastian Fürthauer[2], and Amy S. Maddox[1]

Affiliations

1) Department of Biology, University of North Carolina at Chapel Hill, Chapel Hill, NC, 27599, USA.
2) Institute of Applied Physics, TU Wien, A-1040 Wien, Austria

Correspondence email: asm@unc.edu or fuerthauer@iap.tuwien.ac.at

Key Words: Actomyosin cytoskeleton, Oogenesis, Syncytium, *C. elegans*, Cytokinesis, Active Gel Theory

Summary

The non-muscle actomyosin cytoskeleton generates contractile force through the dynamic rearrangement of its constituent parts. Actomyosin rings are a specialization of the non-muscle actomyosin cytoskeleton that drive cell shape changes during division, wound healing, and other events. Contractile rings throughout phylogeny and in a range of cellular contexts are built from conserved components including non-muscle myosin II (NMMII), actin filaments (F-actin), and crosslinking proteins. However, it is unknown whether diverse actomyosin rings close via a single unifying mechanism. To explore how contractile forces are generated by actomyosin rings, we studied three instances of ring closure within the common cytoplasm of the *C. elegans* oogenic germline: mitotic cytokinesis of germline stem cells (GSCs), apoptosis of meiotic compartments, and cellularization of oocytes. We found that each ring type closed with unique kinetics, protein density and abundance dynamics. These measurements suggested that the mechanism of contractile force generation varied across the subcellular contexts. Next, we formulated a physical model that related the forces generated by filament-filament interactions to the material properties of these rings that dictate the kinetics of their closure. Using this framework, we related the density of conserved cytoskeletal proteins anillin and NMMII to the kinematics of ring closure. We fitted model rings to in situ measurements to estimate parameters that are currently experimentally inaccessible, such as the asymmetric distribution of protein along the length of F-actin, which occurs naturally due to differences in the dimensions of the crosslinker and NMMII filaments. Our work predicted that the role of NMMII varies across these ring types, due in part to its distribution along F-actin and motoring. Our model also predicted that the degree of contractility and the impact of ring material properties on contractility differs among ring types.

Introduction

The non-muscle actomyosin cytoskeleton dynamically remodels to drive numerous cell biological and developmental processes (Bear and Haugh, 2014; Martin, 2020). The abilities of an actomyosin network to rearrange and to generate and resist forces are determined by the interactions among its molecular components: flexible actin filaments (F-actin), bipolar arrays of myosin motors (non-muscle myosin II; NMMII), and non-motor F-actin crosslinkers including anillin, plastin/fimbrin, filamin, and others. Actomyosin rings are specializations of the plasma membrane-associated cortical cytoskeleton that exist in many contexts throughout animal and fungal cell physiology (Green *et al.*, 2012; Schwayer *et al.*, 2016; Cheffings et al., 2016; Pollard and Wu, 2010) . Constricting actomyosin rings drive cell expulsion

from monolayers, healing of multi- or subcellular wounds, enucleation, and cytokinesis (Schwayer *et al.*, 2016). Stable actomyosin rings can maintain cytoplasmic connections among compartments, such as in germline syncytia (see below; (Haglund *et al.*, 2011)).

Cytokinesis, when an actomyosin ring separates the two daughter cells during division, is the context in which the functions of many cytoskeletal proteins including NMMII and anillin scaffold proteins have been defined (Green *et al.*, 2012; Kamasaki *et al.*, 2007; Pollard and Wu, 2010; Pollard and Wu, 2010; Schwayer *et al.*, 2016; O'Shaughnessy and Thiyagarajan, 2018). Anillins are multidomain proteins that bind the plasma membrane and structural and regulatory elements of the actomyosin cytoskeleton (Maddox *et al.*, 2005; D'Avino, 2009; Piekny and Maddox, 2010; Zhang and Maddox, 2010). They contribute to the organization and therefore effectiveness of actomyosin contractile networks (Piekny and Maddox, 2010; D'Avino, 2009; Kučera *et al.*, 2021). NMMII is a motor protein that forms bipolar filamentous aggregates that crosslink and slide F-actin (Glotzer, 2005; Osório *et al.*, 2019; Weeds and Lowey, 1971; Niederman and Pollard, 1975). NMMII is critical for cytokinesis in most animal and fungal cell types (Mabuchi and Okuno, 1977; De Lozanne and Spudich, 1987; Kitayama *et al.*, 1997; Straight *et al.*, 2003; Ma *et al.*, 2012; Pollard, 2017) via its abilities to build stresses by motoring along and crosslinking F-actin (Fang *et al.*, 2010; Ma *et al.*, 2012; Palani *et al.*, 2017; Povea-Cabello *et al.*, 2017; Wang *et al.*, 2020; Osório *et al.*, 2019). NMMII is dispensable for cytokinesis in budding yeast and slime molds due to the dominant mechanical contributions of cell wall deposition and cell motility, respectively (Wloka and Bi, 2012; Lord *et al.*, 2005; Mendes Pinto *et al.*, 2012).

Insight into the mechanisms of actomyosin ring constriction has also come primarily from studying cytokinesis, specifically by measuring closure speed. For example, closure speed scales with ring starting size during *C. elegans* early embryogenesis and vulval precursor cell division, as well as in the filamentous fungus *N. crassa,* such that larger cytokinetic rings close faster than smaller cytokinetic rings and duration is relatively conserved (Carvalho *et al.*, 2009; Calvert *et al.*, 2011; Lan *et al.*, 2019; Bourdages *et al.*, 2014; Khaliullin *et al.*, 2018; Lee *et al.*, 2018). These and other studies support the idea that ring closure arises from constriction of contractile units arranged in series around the ring (Capco and Bement, 1991; Carvalho *et al.*, 2009). By contrast, the distinct kinetics and molecular requirements by different cell types in the same embryo suggest that many different mechanisms exist for contractility (Davies *et al.*, 2018; Ozugergin *et al.*, 2022; reviewed in (Ozugergin and Piekny, 2022)). Thus, while many aspects of actomyosin ring structure and kinetics are widely shared, there exists precedent for mechanistic variations among cell types.

Various approaches to the phenomenological modeling of ring closure have quantitatively recapitulated closure dynamics of cytokinetic rings in *C. elegans*, *S. pombe* (fission yeast), and *S. cerevisiae* (budding yeast) (reviewed in (Cortes *et al.*, 2018; Pollard, 2014)). A subset of these models utilize continuum dynamics to relate cytoskeletal protein density to the kinematics of ring closure (Zumdieck *et al.*, 2007; Turlier *et al.*, 2014; Sain *et al.*, 2015). These models described the relationship between the ring material properties and dynamics of closure without including the role of motor and crosslinker density within the ring and lack the ability to evaluate the behavior of individual component proteins. By contrast, fully discretized physical agent-based models evaluate ring closure from the perspective of the ring's component proteins. These types of models capture ring closure by simulating each of the components within the ring, and evolving those components position over time (Cortes et al. 2022; Nguyen et al. 2018; Vavylonis et al. 2008). A recently developed continuum mechanics model based in active gel theory relates the microscopic interactions of individual filaments to the material properties of a cytoskeletal network (Fürthauer *et al.*, 2019, 2021; Foster *et al.*, 2022).

Actomyosin rings are a conserved feature of germlines which, throughout phylogeny, have a complex syncytial architecture wherein many nucleus-containing compartments are interconnected via cytoplasmic bridges (Koch and King, 1969; Mahajan-Miklos and Cooley, 1994; Kumar and Elkouby, 2023; Pepling and Spradling, 1998). In the *C. elegans* syncytial oogenic germline, hundreds of actomyosin rings

connect nucleus-containing compartments to a central core of common cytoplasm, known as the rachis (Hirsh *et al.*, 1976; Hall *et al.*, 1999). Compartments bear such rings, called rachis bridges, throughout their lifetime. After remaining stably open for tens of hours, a rachis bridge can close if the associated compartment undergoes apoptosis, as do an estimated 50 percent of compartments (Gartner *et al.*, 2008). For compartments that do not undergo apoptosis and instead become oocytes, rachis bridges close when nascent oocytes sever from the syncytium (Hall *et al.*, 1999; McCarter *et al.*, 1999). Since rings throughout the germline syncytium reside in a common cytoplasm and are comprised of the same conserved cytoskeletal components, it could be hypothesized that they operate via a shared mechanism.

We explored the general principles of and variations on non-muscle contractility by quantitatively comparing actomyosin ring closure in germline stem cell mitosis, apoptosis and cellularization. We found that these different actomyosin rings within the *C. elegans* germline exhibit distinct kinetics, as well as profiles of retention of anillin (ANI-1) and NMMII (NMY-2). We utilized a physical framework that relates molecular scale cytoskeletal interactions to the material properties of the ring. Our model suggested that ring closure speed scales not with starting size but with instantaneous size and depends on the material properties of rings, which we found to be dynamic throughout closure and unique to each subcellular context within a large syncytial cell. Our work predicts that differential activity or behavior of NMMII distinguishes the dynamics of these rings from one another.

Methods

Strain maintenance

MDX40 *C. elegans* strain in which mNeonGreen::ANI-1 and mKate2::NMY-2 were expressed from their endogenous loci (ani-1 (mon7[mNeonGreen^3xFlag::ani-1])III x nmy-2(cp52[nmy-2::mKate2+LoxP unc-119(+)LoxP])I; unc-119(ed3) III) was maintained at 20° Celsius using standard methods (Rehain-Bell *et al.*, 2017).

Bacteria-impregnated hydrogel – Mounting Method

Worms were transferred via worm pick into a 1.5 mL tube containing 100 microliters of 0.06% levamisole in S Basal for 10 minutes. 90 - 95 microliters of 0.06% levamisole were removed, leaving the worms in 5 – 10 mL 0.06% levamisole.

Photoactivatable hydrogel solution was prepared as described (Burnett *et al.*, 2018). 2-Hydroxy-4'-(2-hydroxyethoxy)-2 methylpropiophenome (Sigma Aldrich) photoactivator was suspended in S Basal (final concentrations of all components) to create a 0.001% stock ("photoactivator suspension"), and stored at room temperature, covered in aluminum foil. A 10% suspension of Poly Ethelyne Glycol (Acrylate)2 (PEGDA) (VWR, BioMatrix) was prepared in photoactivator suspension. 2 mL of OP50 liquid culture were spun at 5000 rpm for 10 minutes to pellet the bacteria. The bacteria pellet was resuspended into the photo-activator+PEGDA solution.

300 microliters of photoactivator+PEGDA+bacteria suspension was transferred first to the worm-containing tube, and then to a cell culture dish (4-chambered cover glass system #1.5 High-performance cover glass, CellVis, product number: C4-1.5H-N). Worms were pushed to the glass bottom of the dish using an eyelash tool. The dish was then carefully placed on a Speed Light Platinum Gel Documentation system, covered with aluminum foil, and exposed to UV light for 35 seconds to harden the hydrogel. 250 microliters of OP50 liquid culture were pipetted onto the cured gel containing worms.

Fluorescence Imaging

Imaging was performed using a Nikon A1R Confocal Fluorescence Microscope (Nikon) with 1.27 NA 60x water immersion or a 1.41 NA 60x oil immersion lens and a Gallium arsenide phosphide photo-multiplier tube (GaAsP PMT) using Nikon Elements Software and Nikon Perfect Focus.

Ring Dynamic Measurements

Actomyosin ring closure kinetics were measured by cropping the 4-D fluorescence imaging stack around the ring of interest and then performing a sum projection of the focal planes spanned by the ring. Cropped movies were registered by first manually tracking the center of the actomyosin ring using FIJI (Schindelin *et al.*, 2012), and then registering the movies so that the actin ring was in the center of each frame using a custom image registration program written in MATLAB. Rings in registered movies were manually annotated using a custom script in MATLAB. A line was traced around the circumference of the ring as it closed. The pixels covered by the line and the fluorescence intensity within the pixel were recorded. The product of the line length (number of pixels) and pixel size is used as the value for circumference. The total protein was calculated as the sum of the fluorescence intensity of every pixel along the circumference of the ring. The protein density was calculated as the average of the pixels' fluorescence intensity.

Measurements of actomyosin ring circumference were likely underestimates of the true circumference since rings were approximated to lie within an optical section (focal plane). The true measurement is within an approximation of $n\sqrt{2}$ of the measured value, where n was the number of pixels that intersected the actomyosin ring.

Measurements of cytoskeletal ring circumference mNeonGreen::ANI-1 and mCherry-NMY-2 CRISPR (LP229) [nmy-2(cp52[nmy-2::mkate2 + LoxP unc-119(+) LoxP]) I; unc-119 (ed3) III] fluorescence intensity were collected for each actomyosin ring throughout closure for as long as accurate measurements could be made. The accuracy of actomyosin ring circumference measurements decayed as the ring completed closure in all ring types as the diminishing opening in actomyosin rings became diffraction-limited. Thus, ring circumference time series were truncated and underestimated the duration of ring closure time. Circumference time series data were smoothed by an averaging filter computed over 5 time points.

Photo-Bleaching Correction

A photobleaching correction was performed to accurately estimate the change in fluorescence intensity of actomyosin rings over prolonged fluorescence imaging. The decrease in fluorescence intensity was measured in time-lapse image stacks using the Nikon Elements Software package. The measurements of fluorescence intensity were read into MatLab, and a lab-written script was used to correct for fluorescence intensity loss due to photobleaching. The reduction in fluorescence signal was quantified within two regions of interest (ROI); the background, and the dynamic region of interest (where actomyosin rings were measured). The average fluorescence intensity at each frame within each region of interest was tabulated. The background fluorescence intensity was subtracted away from fluorescence intensity values measured from actomyosin rings and the region of interest. An exponential function was fit to the natural logarithm transformed average intensity of the dynamic region of interest to approximate the change in fluorescence intensity due to photobleaching. The ratio method was used to correct photobleaching (Miura, 2020). The corrected fluorescence intensity value was calculated,

$$I_{corrected}(t) = \frac{I_{measured}(t) - I_{background}(t)}{I_{fit}(t)}$$

Where $I_{corrected}(t)$ is the bleach corrected fluorescence intensity at time t, $I_{measured}(t)$ is the measured fluorescence intensity at time t, $I_{background}(t)$ is the fluorescence intensity of the background, and $I_{fit}(t)$ is the exponential fit of the fluorescence intensity in the dynamic range ROI.

Kymograph and Montage Preparation

Kymographs were generated from registered actomyosin ring timelapse movies (see Ring Dynamic Measurement) in Image J using the PlugIn KymographBuilder (Plugins -> Kymograph -> Kymograph Builder). Montages were generated using the Fiji tool Make Kymographs (Image -> Stacks –> Make Montage).

Population circumference and protein fluorescence intensity time alignment

Actomyosin rings within each group were aligned to the final value of each time series; that value corresponds to the last measurement of actomyosin ring circumference made before closure. The time series data for each instance of actomyosin ring closure were truncated to the duration of the shortest acquisition, so that the first time point prior to closure of the population average contained a majority of replicate measurements. The mean value of both circumference and fluorescence intensity at a given time were calculated, along with the standard error. The standard error is calculated as, $standarderror = \frac{\sigma}{\sqrt{n}}$, where σ is the standard deviation of the measurements at time t, relative to the last point measured, and n the number of measurements at time point t relative to the last point measured.

Determination of the start of actomyosin ring closure

Actomyosin ring closure onset was determined by plotting the circumference time series and visually determining the time point after which the circumference curve was clearly and consistently decreasing in value.

Average rate of actomyosin ring closure calculation

The actomyosin ring average circumference change, or closure rate, was calculated as,

$$\frac{dC}{dt} = \frac{C(t=0) - C(t=end)}{T}$$

Where $C(t=0)$ is the circumference at the onset of actomyosin ring closure, $C(t=end)$ is the last measured circumference, and T is the time between the onset of closure and the last measured value of circumference in the time series.

Inferred time to complete closure

The inferred time to complete actomyosin ring closure, assuming that closure rate was constant, is calculated as,

$$T_{complete} = \frac{C(t=0)}{\frac{dC}{dt}}.$$

Where $C(t=0)$ was the actomyosin ring circumference at the onset of closure, $\frac{dC}{dt}$ was the average rate of closure, and $T_{complete}$ is the time in minutes to complete closure.

Actomyosin ring protein content, and protein density time-series alignment to percentage closure

Actomyosin ring protein content and density were aligned by percentage closure. Percentage closure was calculated as,

$$c(t)_{\%} = 100\left(1 - \frac{C(t)}{C(t=0)}\right).$$

Where $C(t)$ is the actomyosin ring circumference at time t, $C(t=0)$ is the actomyosin ring circumference at the onset of closure. The circumferential and fluorescence intensity time series (of both ANI-1 and NMY-2) had the same length, so that the index values of elements in each measurement category corresponded to the same point in time. The sum fluorescence intensity (protein content of every actomyosin ring was then sorted into bins (groups) by percentage closure. The bins contained the associated protein content and density values of 5% increments of closure. The average and standard error of each bin, that contained protein content values organized by percentage closure, was taken.

Actomyosin ring size and rate of ingression scaling analysis

Quantitative relationships between cytokinetic ring circumference at onset of closure and average rate of closure have been reported (Carvalho *et al.*, 2009; Bourdages *et al.*, 2014). This scaling law takes the form,

$$\frac{dC}{dt} = mC_i + b \quad (1)$$

where $\frac{dC}{dt}$ is the average change in circumference throughout closure, C_i is the circumference at the onset of closure, m is a proportionality constant with units $\frac{1}{s}$, and b is the intercept. In *C. elegans* blastomeres, cytokinetic ring closure speed scales with ring size as $m = 0.0038$ and $b = 0$ (Carvalho *et al.*, 2009). When not only blastomeres but also *C. elegans* vulval precursor cells are considered, this relationship is $m = 0.0042, b = -0.02$ (Bourdages *et al.*, 2014). For each cellular context of actomyosin ring closure in the germline, a range of predicted closure rates was determined using the relation from (Bourdages *et al.*, 2014). The lower bound was determined using the mean value and subtracting away the standard error for the value of initial circumference. The upper bound was determined using the mean value plus the standard error for the group initial circumference.

Differential regulation of ANI-1 and NMY-2 turnover rates

We generated a parameterized model to quantitatively express the hypothesis that the turnover rate of protein on each of the actomyosin rings across cellular contexts of closure are the same. If the regulation of turnover rate is different, then the parameter values would be significantly different across cellular contexts. The hypothesis is expressed quantitatively as the change in fluorescence intensity within the rings,

$$\frac{dI}{dt} = k_{on}c(t) - k_{off}I(t) \qquad (2)$$

Where k_{on} is the rate of new protein that associates to the ring per unit time and length, and k_{off} is the fraction of the total protein in the ring that dissociates, per unit time. The product $k_{on}c(t)$ is the total rate of new protein incorporated into the ring, and the product $k_{off}I(t)$ is the total rate of protein lost from the ring. Integration of the rate of change in fluorescence intensity equation provides an estimate of the fluorescence intensity (total protein content) at time t,

$$I(t) = k_{on}\int c(t)dt - k_{off}\int I(t)dt + I_0. \qquad (3)$$

Model Parameterization using Bayesian statistics

Bayesian analysis was used to determine whether the parameterized model (equation 3) provided an adequate description of the observed fluorescence intensity time-series (Neal, 1993; Hoffman and Gelman, 2011; Chib and Greenberg, 1995). The Markov Chain Monte Carlo method with the No U-turn sampling (NUTS) algorithm in the python package PYMC was used to generate distributions for the parameter values k_{on}, k_{off}, for each cellular context of actomyosin ring closure (Patil *et al.*, 2010). The initial protein fluorescence intensity is a spurious parameter since the intensity time-series were normalized to the initial value. The PYMC Bayesian analysis generated the joint likelihood that parameter combinations describe the measured fluorescence intensity time-series for ANI-1 and NMY-2 given the model. The likelihoods of the parameter combinations, and the associated distributions of parameter values, provide a way of comparing the most likely parameter combinations for each context of actomyosin ring closure to one another. The model evaluated here took as input the actomyosin ring circumference and estimated the values of the parameters k_{on}, k_{off} using equation (3).

The MCMC method with the NUTS algorithm was used as above to determine the distribution of parameters values for α^x that described the observed ring closure curves (Figures 1, 5). A separate analysis was performed, as above, to determine joint likelihood of the parameters α^m and $V_{||}$ (Figure 5). The rings studied here were aligned to the last time point measured in each trajectory (see **Population circumference and protein fluorescence intensity time alignment).** The variance among measurements was higher near the onset of closure in apoptotic and cellularizing rachis bridge closure. To account for this, we truncated the first 13 time points from the cellularization data, and the first 10 time points from the apoptosis data (as indicated along the x-axis of Figure 6).

Figures

Graphs, and boxplots were generated in MatLab. All figures were assembled in Adobe Illustrator.

Numerical Programming

Computer programs were written in Matlab and Jupyter Notebook for Python. Source code can be found on Github under the username JackLinehan in the repository Cellular-Context-Specific-Tuning-of-Actomyosin-Ring-Contractility.

Results

Long-term fluorescence imaging of actomyosin ring closure in the *C. elegans* oogenic germline

Cytoskeletal rings are enrichments of F-actin, NMMII, anillin, and diverse other cytoskeletal proteins. These actomyosin rings play a role in a range of cellular processes in addition to canonical cytokinesis. To study contractile force generation in actomyosin rings, we leveraged the co-existence of multiple actomyosin ring closure events in a single syncytial cell: those closing in mitotic, apoptotic, and cellularizing germline compartments in adult *C. elegans* hermaphrodites (Supplemental Movie 1). We first studied the closure of the germline stem cell (GSC) cytokinetic ring during mitosis in the stem cell niche using fluorescently labeled conserved cytoskeletal components anillin 1 (ANI-1) (Figure 1A blue, B, B') and NMMII heavy chain (NMY-2) (Figure 1 C, C'), which enrich on the germline rachis lining, including dynamic

and stable rings. GSC cytokinetic ring closure commenced as soon as enrichment of ANI-1 and NMY-2 was apparent (Figure1 B, C) (Figure 1D, Supplemental Movies 2, 3).

When germline compartments undergo apoptosis, as occurs in approximately 50% of compartments during pachytene of meiosis I prophase (Figure 1A, red) (Gumienny *et al.*, 1999), the rachis bridge closes, separating the compartment from the common cytoplasm. Despite the importance of these rings and the knowledge that they bear many of the same components as other contractile rings, the mechanism of their closure is not known. We next used the same methods to study the closure of actomyosin rings that initially connect apoptotic compartments to the common cytoplasm (Figure E - G). The actomyosin rings associated with apoptotic compartments began as anillin- and NMMII-enriched rachis bridges. After remaining at a roughly constant size for many minutes, they closed at a roughly constant rate (Figure 1 G, Supplemental Movies 4, 5).

In the short arm of the germline, proximal to the spermatheca, nascent oocytes cellularize from the syncytium via closure of their rachis bridge (Figure 1A, green). We also studied rachis bridge closure during the cellularization of nascent oocytes using fluorescently labeled ANI-1 (Figure 1 H, H') to track circumference (Figure 1J) and ANI-1 and NMY-2 abundance (Figure 1 I, I')(Figure 1J, Supplemental Movies 6, 7). As for rings on apoptotic compartments, the rachis bridges that drove cellularization had remained enriched for anillin and NMMII and stably open for some time. Cellularizing rings closed at a roughly constant rate.

In sum, immobilized live, intact adult hermaphrodite *C. elegans* allowed us to observe and measure three distinct types of closing rings in the syncytial oogenic germline.

Kinetics of germline actomyosin ring closure

Insights into the mechanisms of closure by cytoskeletal remodeling and contractile force generation can be gained from measurements of rings 'starting size, closure rate, and closure duration (Carvalho *et al.*, 2009; Calvert *et al.*, 2011). Towards our goal of exploring and comparing closure mechanisms of germline rings, we measured ring size over time in the three contexts (Figure 1 D, G, J). We first compared the initial circumference of rings among groups and found that GSC cytokinetic rings were the smallest ($13.0 \pm 1.2\mu m$; mean plus or minus standard error; Figure 2A), apoptotic germ cell compartment actomyosin rings were approximately 1.4 times larger than GSC cytokinetic rings ($17 \pm 1.6\mu m$; Figure 2A), and cellularizing germ cell compartment actomyosin rings were roughly 1.5 times larger than GSC cytokinetic rings ($21 \pm 1.8\mu m$; Fig. 2A).

The average closure rate was the fastest, at $1.46 \pm 0.1\mu m/minute$, in GSC cytokinetic rings (Figure 2A'). The apoptotic actomyosin ring average closure rate was $0.40 \pm 0.05\mu m/minute$ (Figure 3A'). Cellularizing rings closed at an average rate of $0.44 \pm 0.1\mu m/minute$ (Figure 2A'). We next inferred duration of ring closure by dividing the initial circumference by the average ring closure rate. The average inferred time to close in GSC cytokinetic rings was 9.0 ± 0.70 minutes (Figure 2A''). The average time for the actomyosin ring to close in apoptotic germ cell compartments was 37.0 ± 3.0 minutes (Figure 2A''). The average inferred time to close in cellularizing actomyosin rings was 52.0 ± 8.0 minutes (Figure 2A''). Thus, the speeds and calculated closure times varied among the three contexts in the germline.

Cytokinetic ring kinematics have previously been explained by a scaling law relating the initial circumference to closure rate (Carvalho *et al.*, 2009; Calvert *et al.*, 2011; Bourdages *et al.*, 2014; Calvert *et al.*, 2011). We explored whether starting ring size was sufficient to predict closure speed for the three *C. elegans* germline ring types (Figure 2 B, B')(see Materials and Methods). The measured rate of GSC cytokinetic ring closure indeed fell within the range of closure speed predicted by starting size. This finding suggested that rings in at least three contexts of cytokinesis share mechanisms. By contrast, the measured rates of ring closure for apoptotic or cellularizing rachis bridges were substantially lower than what was predicted by the relationship between initial ring circumference and rate of closure for other *C. elegans*

cell types (Figure 3B'). Thus, rachis bridges either close via distinct mechanisms, or close via the same shared mechanism as do cytokinetic rings, but experience greater forces opposing constriction.

Despite the compatibility of the scaling argument for cytokinesis in GSCs and other cell types, the relationship between the initial ring circumference and closure rate derived from measurements of blastomeres overestimated the measured GSC cytokinetic ring closure rates by roughly a factor of two (predicted rate of closure $0.045\frac{\mu m}{s}$; measured rate of closure $0.024\frac{\mu m}{s}$) (Carvalho *et al.*, 2009). An adjusted relationship that includes both embryonic and vulval precursor cell cytokinesis data predicts that GSC rings close at $0.03\frac{\mu m}{s}$, which is closer to the measured value of $0.024\frac{\mu m}{s}$ (Figure 2B') (Bourdages *et al.*, 2014). The earlier quantification of the relationship between ring speed and closure rate implied a direct scaling, while the latter utilized a linear relationship. In total, this analysis revealed that the kinetics of GSC cytokinesis differ from rachis bridge closure in both apoptotic germline compartments and cellularizing nascent oocytes. The finding that germline rachis bridges closed more slowly than predicted by the scaling relationship between initial circumference and closure speed suggests that: 1) forces resisting ring closure are higher in the rachis lining than in GSCs, or 2) rachis bridges and cytokinetic rings contract via different mechanisms.

Time independent ANI-1 and NMY-2 evolution distinguishes the GSC cytokinetic ring from the rachis bridges

The dynamics of the abundance of ring components over the course of ring closure varies among components and across organisms; compaction and retention dominate some systems, whereas protein density remains relatively constant in other cell types (Wu and Pollard, 2005; Mendes Pinto *et al.*, 2012; Khaliullin *et al.*, 2018; Okada *et al.*, 2021). *In silico* modeling demonstrated that protein abundance dynamics (recruitment, retention, and loss) of key structural components strongly influences the kinetics of actomyosin ring closure (Cortes *et al.*, 2022). We reasoned that differences in protein abundance over the course of ring closure among the three ring types would be evidence that the ring types close via unique mechanisms. By contrast, highly similar fold changes in ring component abundance among ring types would suggest a consistent ring-intrinsic mechanism of closure.

To study the evolution of the three germline ring types independent of the kinematic differences reported above, we measured the fold change of the abundance of the conserved cytoskeletal proteins ANI-1 and NMY-2 as a function of percentage closure. To interpret our protein abundance measurements, we calculated density change for various theoretical regimes of recruitment, retention, and loss (Figure 4 A, A'). If the net amount of protein is constant throughout closure, we would expect a 5-fold increase in density when the ring is 80% closed (Figure 4 A, A'; purple). If protein is lost at a rate that is exactly equal to the rate of closure, then the density would remain constant (Figure A, A'; pink). A fold change in density greater than 5x indicates a net gain in the ring, and a fold change that is between 1x and 5x corresponds to a partial loss of protein.

Normalized fluorescence density and abundance of tagged ANI-1 and NMY-2 varied among the three ring types. GSC cytokinetic rings experienced a greater fold change in density of ANI-1 and NMY-2 than the rachis bridges, which exhibited similar fold changes (Figure 3 B', C'). ANI-1 abundance initially increased during GSC cytokinesis, and around 50% closure began to decrease. In rachis bridges, ANI-1 was lost throughout closure (Figure 3B). NMY-2 abundance increased in GSC cytokinetic rings and decreased in both rachis bridges (Figure 3C). Our measurements of ring protein abundance suggest that these dynamics are determined by ring type or cellular context; such a difference in contractile regulation may underlie kinetic differences.

Time dependent ANI-1 and NMY-2 abundance dynamics differ among subcellular contexts of actomyosin ring closure

The total abundance and average density of ANI-1 and NMY-2 diverged among ring types as they closed (Figure 3). Given that the time to complete ring closure varied several fold across subcellular contexts, we next asked how protein abundance varied in time. Furthermore, we leveraged these time-resolved abundance measurements to estimate turnover rates for each protein in each ring type. We used a generalized model for the change in protein content over time:

$$\frac{dI}{dt} = k_{on}C(t) - k_{off}I(t) \qquad (2)$$

where material incorporation was the product of k_{on} (the rate of protein added per unit space per unit time) and the current circumference of the ring $C(t)$ and material loss was the product of k_{off} (the fraction of ring protein shed per unit of time) and the current protein content, $I(t)$ (Figure 4A). We calculated the likelihood that the measured fluorescence intensity time-series data were generated by the linear model given a normally distributed error. The Markov Chain Monte Carlo (MCMC) method was used to determine the distribution of parameters k_{on} and k_{off} that fit each average fluorescence intensity over time curve. As expected, the predicted fluorescence intensity time series calculated from the mean parameter values for k_{on} and k_{off} (Figure 4 B, C) agreed well with our measured fluorescence intensity time series. The distributions of the parameter value k_{on} and k_{off} were well separated (Figure 4 B', C'). These results suggest that the regulation of both ANI-1 and NMY-2 differs among the three ring types studied here. Together, our findings indicate that context-dependent actomyosin ring kinetics arise from differences in mechanisms of contractility, independent of any difference that may exist in external force opposing constriction.

Theory for actomyosin rings

The similarities in ring makeup (all contain F-actin, NMMII, and non-motor crosslinkers including anillin (as reviewed in (Schwayer *et al.*, 2016)) suggested that a unified theoretical framework could help us explore the differences in their mechanisms of contractility. We used a theoretical physical framework that relates molecular scale interactions to filament network material properties (Fürthauer *et al.*, 2021; Fürthauer *et al.*, 2019). The theory derives contractility kinetics from component abundance, beginning with a description of the forces acting on actin-like filaments filament i due to interactions with neighboring filament j via connections made by crosslinkers representing non-motor crosslinkers including anillin, and motors representing NMMII (Figure 5B).

$$f_{ij}^{x} = -\gamma^{x}c^{x}(s_i, s_j)(\vec{v}_i + s_i\dot{\vec{p}}_i - \vec{v}_j - s_j\dot{\vec{p}}_j), \qquad (4)$$

is the force on actin filament i due to interactions via crosslinkers, and

$$f_{ij}^{m} = -\gamma^{m}c^{m}(s_i, s_j)(\vec{v}_i + s_i\dot{\vec{p}}_i - \vec{v}_j - s_j\dot{\vec{p}}_j + V_{||}(\vec{p}_i - \vec{p}_j)). \qquad (5)$$

is the force due to interactions with neighboring filaments via motors. The coefficients γ^x, γ^m are the friction constants of crosslinkers x and motors m. The terms $\vec{v}_i, \vec{v}_j$ describe the velocity of the respective filaments. $c^x(s_i, s_j), c^m(s_i, s_j)$ is the density of crosslinkers and motors bound between points s_i on filament i and point s_j on filament j. The parameters $\vec{p}_i, \vec{p}_j$ are the unit vectors describing the direction filaments are oriented (Figure 5A). $V_{||}$ is the motor stepping speed, taken to be $150\,\frac{nm}{s}$ (Nagy *et al.*, 2013).

As previously shown (Fürthauer *et al.*, 2021), we can without loss of generality, approximate the crosslink and motor densities by the linear functions of s_i, s_j, such that

$$c^x(s_i, s_j) = c_0^x + \alpha^x c_0^x (s_i + s_j) L^{-1} \qquad (6)$$

$$c^m(s_i, s_j) = c_0^m + \alpha^m c_0^m (s_i + s_j) L^{-1} \qquad (7)$$

where $c_0^{x,m}$ is the total amount of crosslinker or motor along the length of the filament, $\alpha^x c_0^x$ and $\alpha^m c_0^m$ quantifies the spatial asymmetry of the crosslinking and motor proteins 'distribution along the length of filaments (Figure 5B).

Starting from the above molecular detail equations, and following the coarse graining procedure in NJP, we derived the macroscopic material properties of the network. The network stress obeys

$$\Sigma = \eta_s \left[\nabla \vec{v} + \left(\nabla \vec{v} \right)^T + \nabla \cdot \vec{v} \right] + \Sigma^A I \qquad (8)$$

where $\vec{v}$ is the mean network velocity and I is the identify matrix. η_s is the viscosity, given by

$$\eta_s = \frac{4\pi R^3}{15} \rho^2 (\gamma^x c_0^x + \gamma^m c_0^m)(\frac{R^2}{5} + \frac{L^2}{54}) \qquad (9)$$

where $L = 500nm$ is the length of the filaments (Wu and Pollard, 2005; Courtemanche *et al.*, 2016; Cortes *et al.*, 2022), the crosslinker and motor bridge filaments with a distance $R = 13nm$, and ρ is the density of F-actin. The active stress in the network is

$$\Sigma^A = -\frac{4\pi R^3}{27} \frac{L^2}{12} \rho^2 \gamma^m V_{||} \frac{\alpha^m c_0^m \gamma^x c_0^x - \alpha^x c_0^x \gamma^m c_0^m}{\gamma^m c_0^m + \gamma^x c_0^x}, \qquad (10)$$

Where we assumed that filaments in the ring would be aligned along the ring.

The stress and force balance equations are applied to a ring parameterized by the angle θ, such that the arc length s is $s = r\theta$; where r is the ring radius. We assume that the cytoskeletal network is a thin ribbon with thickness h (Figure 5A). Next, we define the normal vector $\hat{e}_z$ and the tangent vector $\hat{e}_s$ (Figure 5A). We now write the force balance $\nabla \cdot \Sigma = 0$ for this geometry given the thin shell approximation $h \ll r$,

$$\eta_s \frac{1}{r^2} \left(\partial_\theta^2 V^s + \partial_\theta V^z \right) + \frac{1}{r} \partial_\theta \Sigma^A - \gamma V^s = 0 \qquad (11)$$

for the tangential direction force balance equation and

$$\frac{\eta_s}{r^2} (\partial_\theta V^s + V^z) + \frac{1}{r} \Sigma^A = 0 \qquad (12)$$

is the radial direction force balance equation. V^s is the tangential velocity along the ring circumference opposed by external friction γ due to interactions with the plasma membrane and actomyosin cortex. V^z is the normal velocity which induces changes in the radius r. We assume that γ is sufficiently large so that $V^s = 0$. The dynamics of the ring system are found by deriving the solution to equation (12),

$$\frac{dr}{dt} = -r\frac{\Sigma^A}{\eta_s} \qquad (13)$$

where $V^z = \frac{dr}{dt}$ is the radial velocity at a point along the circumference of the ring.

By implementing equations (9) and (10) in (13) we have

$$\frac{dr}{dt} = A_0\gamma^m V_{||} r \frac{\alpha^m c_0^m \gamma^x c_0^x - \alpha^x c_0^x \gamma^m c_0^m}{\left(\gamma^x c_0^x + \gamma^m c_0^m\right)^2} \qquad (14)$$

where $A_0 = \frac{5L^2}{108(\frac{R^2}{5}+\frac{L^2}{54})}$. Equation (14) relates the changes in protein abundance within rings to the kinematics of ring closure in the absence of an external force.

We note that the derivation of the model presented in Equations 4-14 assumed isotropic actin filament orientations in the ring, for simplicity. An alternative hypothesis, that the cytoskeleton has strong nematic alignment within the ring, leads to the same final form of Equation 14, but $A_0 = \frac{15L^2}{108(\frac{R^2}{5}+\frac{5L^2}{36})}$. For the following, we used A_0 from the isotropic case. Importantly, none of the conclusions of this work depended on this choice (derivation not shown).

The asymmetric distribution of cytoskeletal components along actin-like filaments is sufficient to recapitulate observed ring closure trajectories

To understand what microscopic details of network architecture determine the kinetics of actomyosin ring closure, we considered the distribution of the crosslinker and the motor along the length of actin-like filaments represented in the theory. We first assessed a minimal model wherein either the crosslinker or motor was asymmetrically distributed along the length of filaments. To focus our current work on the effects of the abundance of motor and crosslinker, we set the value for friction (g; proportion bound) $\gamma^x = \gamma^m$. The equation of motion for a single asymmetry a was given by

$$\frac{dr}{dt} = A_0\gamma^{m,x}\gamma^m V_{||} r \frac{\mp\alpha^{x,m} c_0^{x,m} c_0^{m,x}}{\left(\gamma^x c_0^x + \gamma^m c_0^m\right)^2}. \qquad (15)$$

We first considered the case in which the motor is equally distributed along the length of filaments $\alpha^m c_0^m = 0$, while the distribution of the crosslinker was biased towards the filament plus end $\alpha^x c_0^x > 0$. To determine the extent to which a crosslinking protein would need to be asymmetrically distributed to cause closure, we used $\frac{dr}{dt} = A_0(\gamma^m)^2 V_{||} r \frac{-\alpha^x c_0^x c_0^m}{\left(\gamma^x c_0^x + \gamma^m c_0^m\right)^2}$ (equation 15). We used the MCMC method to determine the distribution of parameter values of α that related the measured protein density dynamics to the observed ring closure curves (Figure 5A; black: model predicted curves using the mean α value). For germline stem cell cytokinesis, $\alpha^x = 0.033 \pm 0.0006$ allowed a good fit to the observed ring closure kinetics (Figure 6A, A'). For apoptotic or cellularizing actomyosin ring closure, $\alpha^x = 0.011 \pm 0.0003$, and $\alpha^x = 0.005 \pm 0.0002$ $(mean \pm std)$ provided sufficient estimates, respectively (Figure 6 A, A'). Thus, the MCMC method revealed that measured ring kinetics could be fit well with unique α values for each of the three ring types, providing further support for the idea that the three ring types close via distinct mechanisms.

Next, we considered the case that the crosslinker was equally distributed along the length of filaments $\alpha^x c_0^x = 0$, while the distribution of the motor was biased towards one end of the filament. These conditions resulted in equation (15) having the form, $\frac{dr}{dt} = A_0\gamma^x\gamma^m V_{||} r \frac{\alpha^m c_0^m c_0^x}{\left(\gamma^x c_0^x + \gamma^m c_0^m\right)^2}$, for the ring

to close $\alpha^m c_0^m < 0$. Since we had defined $\gamma^x = 1$, the absolute value of this expression was the same as was evaluated above for $(\alpha^x \neq 0, \alpha^m = 0)$, but of opposite sign. The minimal model yields $\alpha < 0$ when the motor is asymmetrically distributed along F-actin, and $\alpha > 0$ when the crosslinker is considered asymmetric; the absolute value of the distribution of α was the same.

In summary, these results validate the relationships among individual component behavior, the material properties of the ring, and the kinetics of closure modeled in equations 4-14 as sufficient to recapitulate the dynamics of actomyosin ring closure.

The material properties of actomyosin rings change throughout closure

Active stress and viscosity are material properties of actomyosin networks that dictate the kinetics of their contractility. These important characteristics are difficult to directly measure experimentally, but they can be estimated using our theoretical framework. To understand how the changing protein densities dictate the material properties of these rings, we calculated the active stress and viscosity for each ring type using the mean value of the asymmetry parameter distributions using equations (9) and (10) (Figure 6A', evaluated at $\alpha^m = 0$). (Because asymmetric distribution of either the non-motor crosslinker or the motor was sufficient to fit the model to our kinetics measurements (see Fig. 6A), the results of our exploration of the material properties of the ring, are equivalent when either $\alpha^x c_0^x = 0; \alpha^m c_0^m \neq 0$ or $\alpha^m c_0^m = 0; \alpha^x c_0^x \neq 0$.) Since not only the starting state, but also in the dynamics of kinetics and protein abundance changed over the course of ring closure, we calculated how active stress and viscosity evolved over time. Active stress and viscosity grew in each of the cellular contexts of closure, with cytokinesis growing 10-fold more than apoptosis, and 50-fold greater than in cellularization (Figure 6B, B'). These findings revealed that the material properties of germline rings during closure were dynamic, and unique to each cellular context.

Actomyosin ring contractility exhibits unique dynamics across subcellular contexts

Our physics-based framework revealed that closure speed is due to two distinct parameters, a ring's size and its material properties ($\frac{dr}{dt} = -r\frac{\Sigma^A}{\eta_s}$). Both active stresses and viscosity can be dynamic, so the dynamics of ring closure could result from the constant or dynamically evolving value of one or both of these factors. To calculate and compare contractility, independent of ring size, for our rings, we next determined the contractility, defined as $\frac{\Sigma^A}{\eta_s}$, from equation (13) for each ring type. We found that the GSC cytokinetic ring experienced a $\sim 10\%$ reduction in contractility during closure (Figure 6 C; blue). Apoptotic compartment rings experienced a similar, but more gradual, reduction in contractility (Figure 6 C; red). By contrast, in cellularization rings, contractility remained constant throughout closure (Figure 6C; green). Together, these results showed that the mechanism of ring closure was the same across the three cellular contexts. The dynamics of closure diverged amongst groups due to the cellular context specific regulation of protein abundance within the rings.

The magnitude of the active stress may vary across subcellular contexts due to differences in force production by the motor

Above, we estimated contractility using measured molecular component densities and a single free parameter, α, the asymmetry of protein distribution along the length of the F-actin like filaments (equation 15; Figure 6A, A'). For that work, we held another key parameter constant: the velocity of NMMII motoring ($V_{||}$). While good estimates of $V_{||}$ exist (Nagy *et al.*, 2013; Cuda *et al.*, 1997), NMMII motoring speed varies across conditions including load (Lord *et al.*, 2005; Wloka and Bi, 2012; Stam *et al.*, 2015; Guo and Guilford, 2006). We hypothesized that $V_{||}$ could vary among germline ring types.

We tested this hypothesis using the MCMC method to calculate the motor protein distribution asymmetry (α) and the motor speed $V_{||}$. We found that α^m, $V_{||}$, and their product $|\alpha^m| * V_{||}$ varied among the subcellular contexts (Figure 6 D, D'). $|\alpha^m|$ and $V_{||}$ were inversely related (Figure 6D), indicating that these two parameters provide the means of tuning motor-based force production. For a given value of $|\alpha^m|$, $V_{||}$was always higher, and vice versa, for the GSC rings than for either type of rachis bridge, suggesting that NMMII contributes more to the closure of GSC rings than rachis bridges. Together, these results indicate that the motoring speed, and contribution to contractility, of NMMII varies across subcellular contexts.

Discussion

To explore how contractility emerges from the cytoskeletal interactions within non-muscle actomyosin networks, we studied three instances of actomyosin ring closure within a large syncytial cell. We observed actomyosin rings closing in germline stem cell cytokinesis, the closure of apoptotic compartments, and the cellularization of nascent oocytes. We found that the kinetics of ring closure varied amongst the three groups, and that the conserved cytoskeletal proteins anillin and non-muscle myosin II were differentially retained across contexts. This indicated that the rings closed via unique strategies. We generated a physical model that related protein density dynamics and closure kinetics to the material properties of these rings. This framework allowed us to quantitatively predict the behavior of ring components and compare the predictions across the three rings. Our model revealed that the material properties of actomyosin rings are dynamic throughout closure, and predicted that the role of myosin motoring varies across contexts (Figure 6). Together, our measurements and physical modelling NMMII ring closure indicate that ring closure results from cellular context-specific tuning of ring contractility ($\frac{\Sigma^A}{\eta_s}$) via regulation of the density of component proteins within rings and the asymmetric distribution of crosslinking and motor proteins along F-actin. Our data suggest that the role of NMMII varies amongst these contexts, potentially due to differences in its ring recruitment kinetics.

Physical modeling and observations of ring closure motivate testable hypothesis of ring contractility

Our assumption that NMMII abundance scales with the abundance of F-actin, as has been observed (Mendes Pinto *et al.*, 2012; Cortes *et al.*, 2022; Wu and Pollard, 2005; Okada *et al.*, 2021), largely dictated the relationship between the ring active stress and viscosity (Figure 6 B-B'; equations (9) and (10)). Additionally, we calculated inferred turnover rates from our measured protein (NMMII and anillin) abundance time series for each context of ring closure. These data indicated that the differential retention of both ANI-1 and NMY-2 across subcellular contexts could be due to cellular context specific turnover of these proteins within rings. Our results motivate several measurements including that of F-actin abundance throughout ring closure, and of the turnover (or fluorescence recovery after photobleaching (FRAP) of conserved cytoskeletal proteins. Interestingly, our work indicated that the GSC cytokinetic ring generated more active stress than either of the rachis bridges. Laser ablation of rings can be used to measure recoil velocity and compare the relative magnitude of ring intrinsic forces during closure among ring types. In addition, our modeling work indicated that NMMII motoring contributed more to the closure of the GSC cytokinetic ring than to the closure of rachis bridges. Genetically tuning NMMII motor activity (*e.g.* via the use of a *C. elegans* strain expressing temperature-sensitive NMMII mutant) could help test whether GSC cytokinesis is more sensitive to temperature shifting than apoptosis and cellularization.

The magnitude of contractile stress generated by the rings varied across subcellular contexts

The rate of ring closure in GSC cytokinesis was accurately predicted using a size-speed scaling relationship with both embryonic and larval somatic *C. elegans* cell types, indicating that the mechanics

of cytokinesis are broadly conserved across cell type and size at least within this species. Interestingly, the same relationship failed to predict the observed closure rates of the two types of rachis bridges. We leveraged our model to test the published explanation for size-speed scaling: the "contractile unit hypothesis" that speed is a function of the number of cytoskeletal segments arranged in series around the ring, corresponding to the starting circumference (Capco and Bement, 1991; Carvalho *et al.*, 2009). We found that across the three ring types the rate of closure was dependent not on the initial circumference but on instantaneous size r, the ring radius, and that the proportionality constant was determined by the material properties of the actomyosin ring ($m = \frac{\Sigma^A}{\eta_S}$, equations 1, and 13) rather than the starting amount of its constituent components. The independent representation of material properties and ring size was necessary for our framework (Equation 13) to recapitulate observed kinetics. We can recover the size scaling relationship using equation 15 if larger cytokinetic rings have 1) the same parameter values and 2) similar protein kinetics, as we observed in the GSC cytokinetic ring. The relationship then for ring size and closure rate using our framework is $\frac{dr}{dt} = \Omega r$ where $\Omega = A_0 \gamma^m V_{||} \frac{\alpha^m c_0^m \gamma^x c_0^x}{(\gamma^x c_0^x + \gamma^m c_0^m)^2}$. Thus, in keeping with the contractile unit or "horse-power" hypothesis, the dimensions of a contractile array are important, but material properties, which vary not only among ring types but over time within a ring type, are also key to explaining contractile speed (Figure 6B).

The asymmetric distribution of NMMII along F-actin and its motoring tune ring contractility

Non-motor crosslinkers including anillin can generate contractile forces in reconstituted F-actin networks but only when the level of filament overlap is low (Kučera *et al.*, 2021); in cytokinetic rings F-actin is thought to be maximally overlapped (Swulius *et al.*, 2018; reviewed in (Mangione and Gould, 2019)). Therefore, we assumed that the non-motor crosslinker contributes minimally to contractility. *In vivo* and in our model, NMMII generates contractile stresses via motoring and contributes to network viscosity by crosslinking F-actin (Wang *et al.*, 2020). The contribution of NMMII motoring to ring closure *in vivo* varies across organismal contexts (Lord *et al.*, 2005; Osório *et al.*, 2019; Wloka and Bi, 2012) and could vary among the three subcellular contexts we explored. Since the magnitude of the force generated by NMMII depends on both its polarized distribution along filaments and its motor activity (Equation 5), it could be that either the asymmetric distribution, degree of filament sliding, or a combination of both contributed to tuning the contractility of rings across cellular contexts.

The asymmetric distribution of crosslinking and motor protein along F-actin is a physical inevitability

Our work indicates that the asymmetric distribution of crosslinking and motor protein results in contractile stresses within the ring. The interactions between cytoskeletal proteins are known to directly impact network architecture (reviewed in (Kadzik *et al.*, 2020)). Asymmetry likely naturally occurs given that NMMII forms bundles that span larger distances between actin filaments than many individual crosslinking proteins (Sinard *et al.*, 1989). For example, the crosslinking proteins fascin and α-actinin segregate due to differences in size, resulting in mutually exclusive binding of F-actin due to the space between filaments within bundles (Winkelman *et al.*, 2016; Li *et al.*, 2015). Thus, it is likely that cytoskeletal proteins occupy mutually exclusive (asymmetric) zones along actin filaments within actomyosin rings.

During closure, rings become increasingly viscous, which reduces contractility

Our measurements and modeling suggest that as the density of molecular components increases, the ring becomes increasingly viscous, and therefore less contractile (Figure 6 B-B', C). Thus, the model predicts that the GSC cytokinetic ring and apoptotic compartment ring slow near to 80% closure, as is

observed in the cytokinetic ring of the *C. elegans* zygote (Carvalho *et al.*, 2009; Dorn *et al.*, 2016; Khaliullin *et al.*, 2018; Cortes *et al.*, 2022). In contrast, contractility of rachis bridges on cellularizing oocytes was constant throughout closure and was associated with a lower measured density of NMMII and inferred motoring speed. The abundances of ANI-1 and NMY-2 in cellularizing rings trended similarly throughout closure as the homologous proteins' abundances in budding yeast, where cell wall deposition contributes to ring closure. Cellularization occurs on a tapered conical surface; this geometry may contribute to the closure of rachis bridges during cellularization.

In sum, our theoretical model implementing in vivo measurements reveals that different rings in a syncytium close via the same mechanics but with distinct regulation of protein component density, abundance, and distribution. Our framework makes many testable hypotheses about how protein behavior and abundance dynamics, material properties, and the kinetics of actomyosin ring closure are linked.

Acknowledgements

We thank all members of our labs for fruitful discussions and helpful reading of the manuscript. We thank Emily Bartle for help with image registration method. SF and AZ have been funded by the Vienna Science and Technology Fund (WWTF)[10.47379/VRG20002]. JBL was supported in part by a grant from NIGMS under award T32 GM119999. This study was also supported by the NIGMS of the National Institutes of Health (R35GM144238), and by the National Science Foundation (2153790) to ASM.

Author Contributions

ASM, PSM, MEW, BH, JBL conceived and designed experiments and methods. JBL performed experiments and analyzed data, BH and MEW provided technical support for those experiments and analysis. AZ and SF formulated model. JBL implemented model. JBL, AZ, MEW, BH, PSM, SF, and ASM contributed to writing and editing of the manuscript.

FIGURES

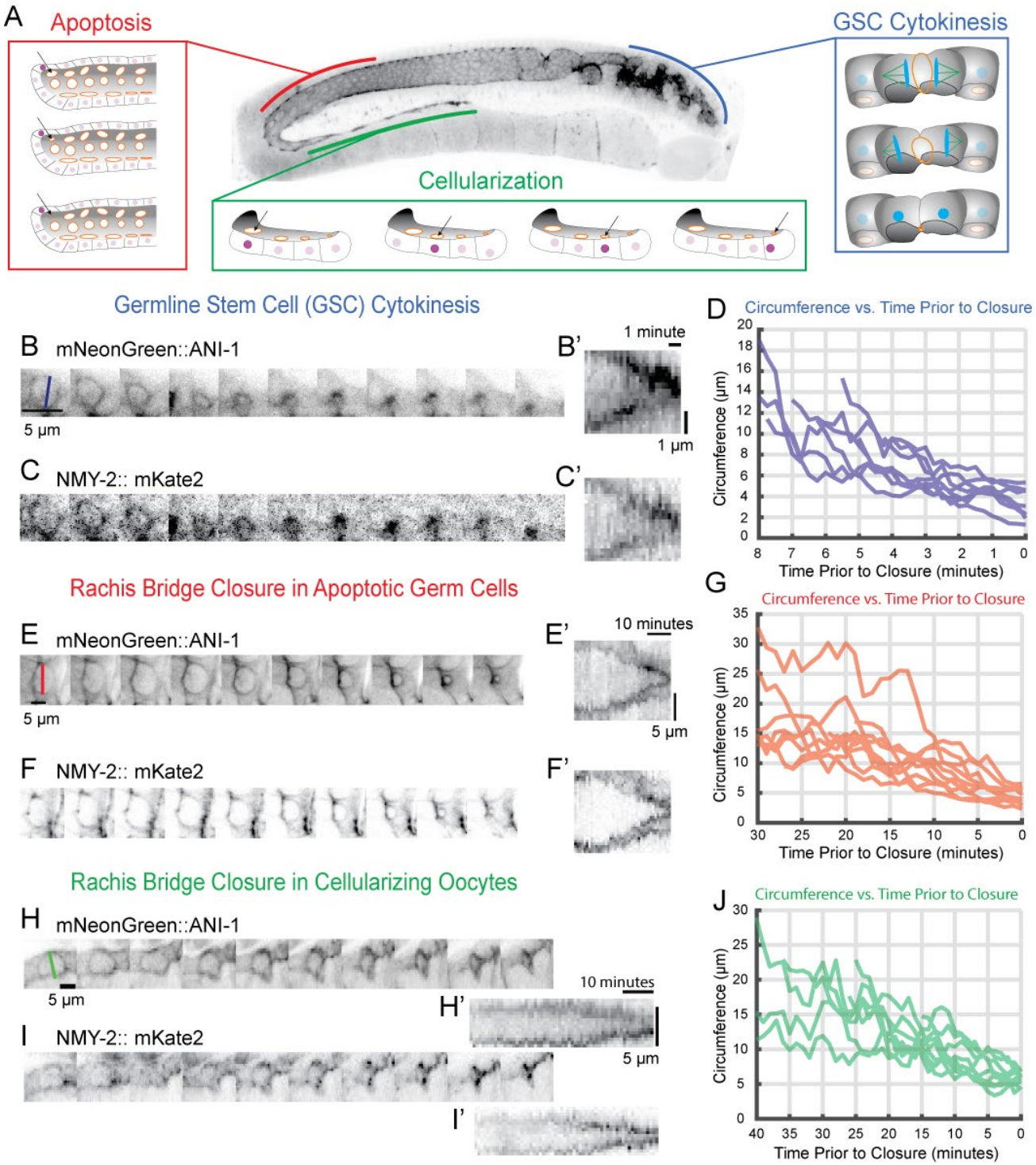

Figure 1: Actomyosin ring closure varies qualitatively and quantitatively among ring types in the *C. elegans* oogenic syncytial germline. A) The oogenic germline with brackets indicating the locations where germline stem cell (blue), apoptotic (red), and cellularizing nascent oocyte (green) actomyosin ring closure occur. B, E, H) ANI-1 sum fluorescence intensity image montages of actomyosin rings in each cellular context. B', E', H') Kymographs of actomyosin ring closure generated from ANI-1 fluorescence sum projections. C, F, I) Non-muscle myosin II sum fluorescence intensity montages showing actomyosin ring closure in germline stem cell cytokinesis (C), apoptotic cell compartments (F), and cellularizing nascent

oocytes (I). C', F', I') Kymographs generated from non-muscle myosin II imaging. D, G, J) Actomyosin ring circumferential time series, $mean \pm se$; each actomyosin ring trajectory was aligned to the final point in its trajectory. D) GSC cytokinesis, G) apoptotic compartment rachis bridge closure, J) cellularizing nascent oocyte rachis bridge closure.

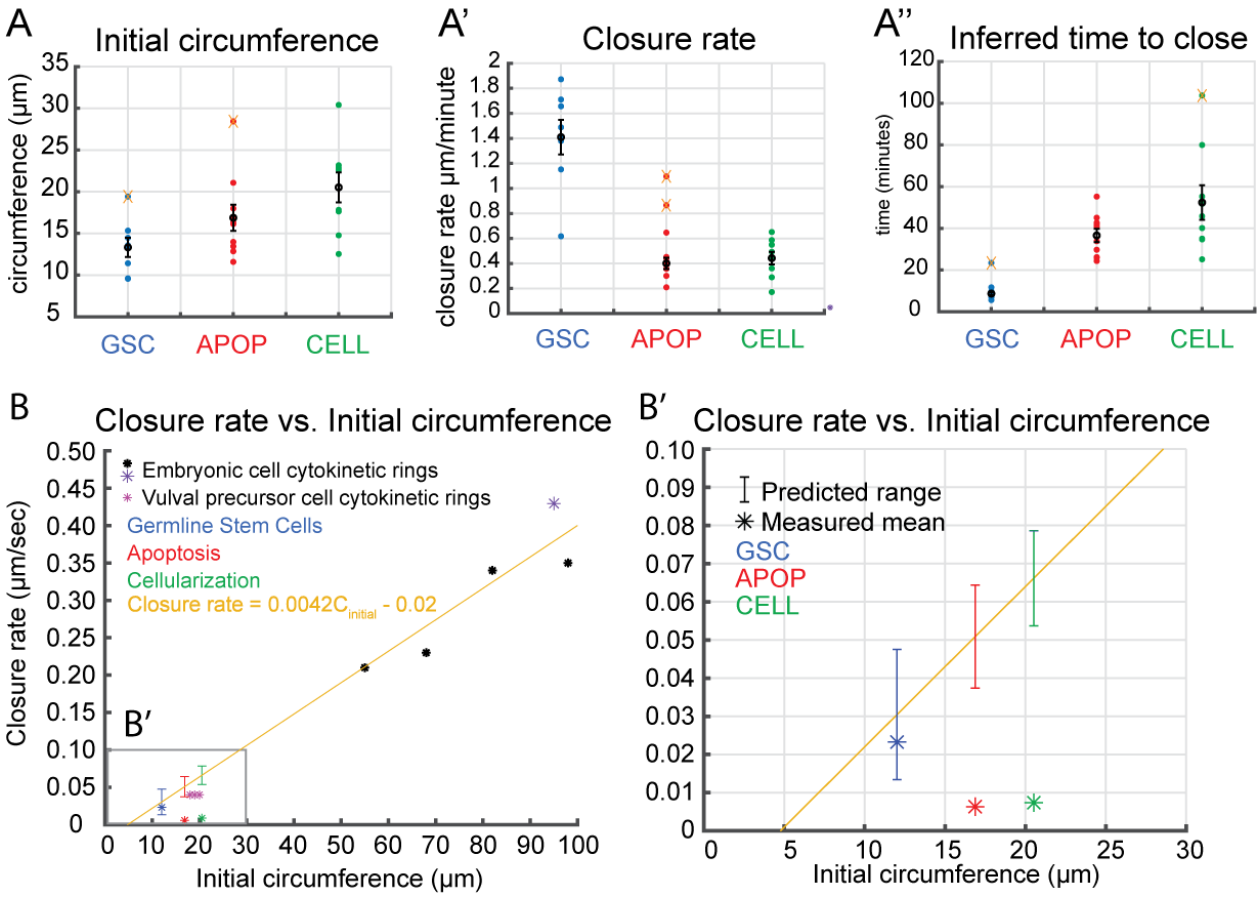

Figure 2: Comparison of actomyosin ring closure in mitotic germline stem cells, apoptotic, and cellularizing germ cell compartments. A) Actomyosin ring circumference at the onset of closure. A') Actomyosin ring closure rate. A'') The inferred time to close. B) Starting ring size and closure rate for multiple *C. elegans* cell types. Closure rates for embryonic stage cytokinesis and cytokinesis in vulval precursor cells were derived from the literature (Carvalho et al. 2009)(Bourdages et al. 2014) B') Predictions of actomyosin ring closure rates based on actomyosin ring scaling relationship; brackets: range of expected ring closure speed; blue, GSC cytokinetic rings; red, apoptosis; green, cellularization.

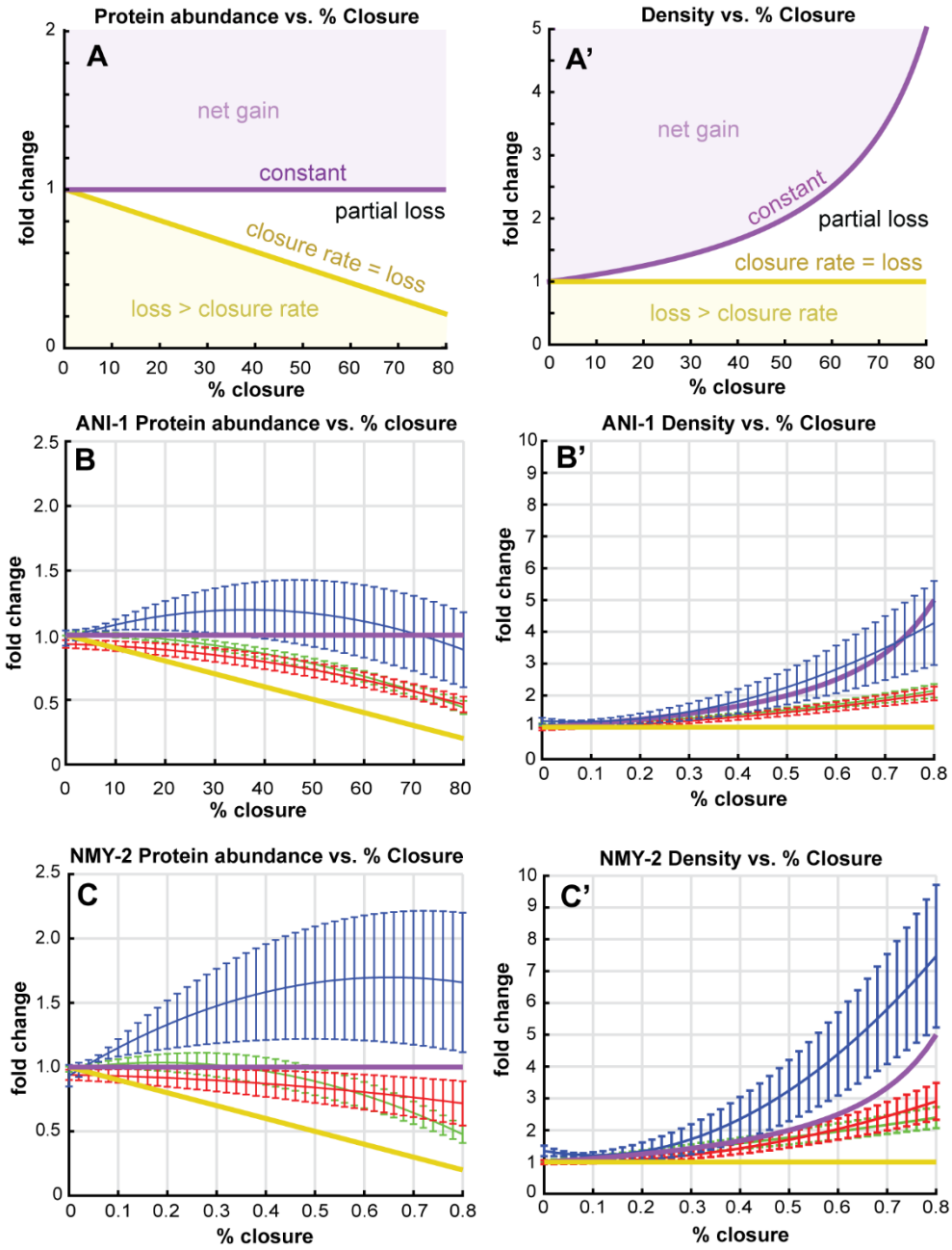

Figure 3: ANI-1 and NMY-2 density and abundance during closure. A, A') Limiting cases of protein turnover; A': expected fold change in protein abundance as the ring closes given a net gain in protein (light purple), constant abundance (purple), fractional loss (white), equivalency between protein change and circumference change (yellow), and when protein loss is greater than rate of closure (light yellow). B) ANI-1 abundance as a function of percent closure; GSC cytokinesis (blue), apoptosis (red), cellularization (green). B') ANI-1 density as a function of percent closure. C) NMY-2 abundance as a function of percent closure. C') NMY-2 density as a function of percent closure.

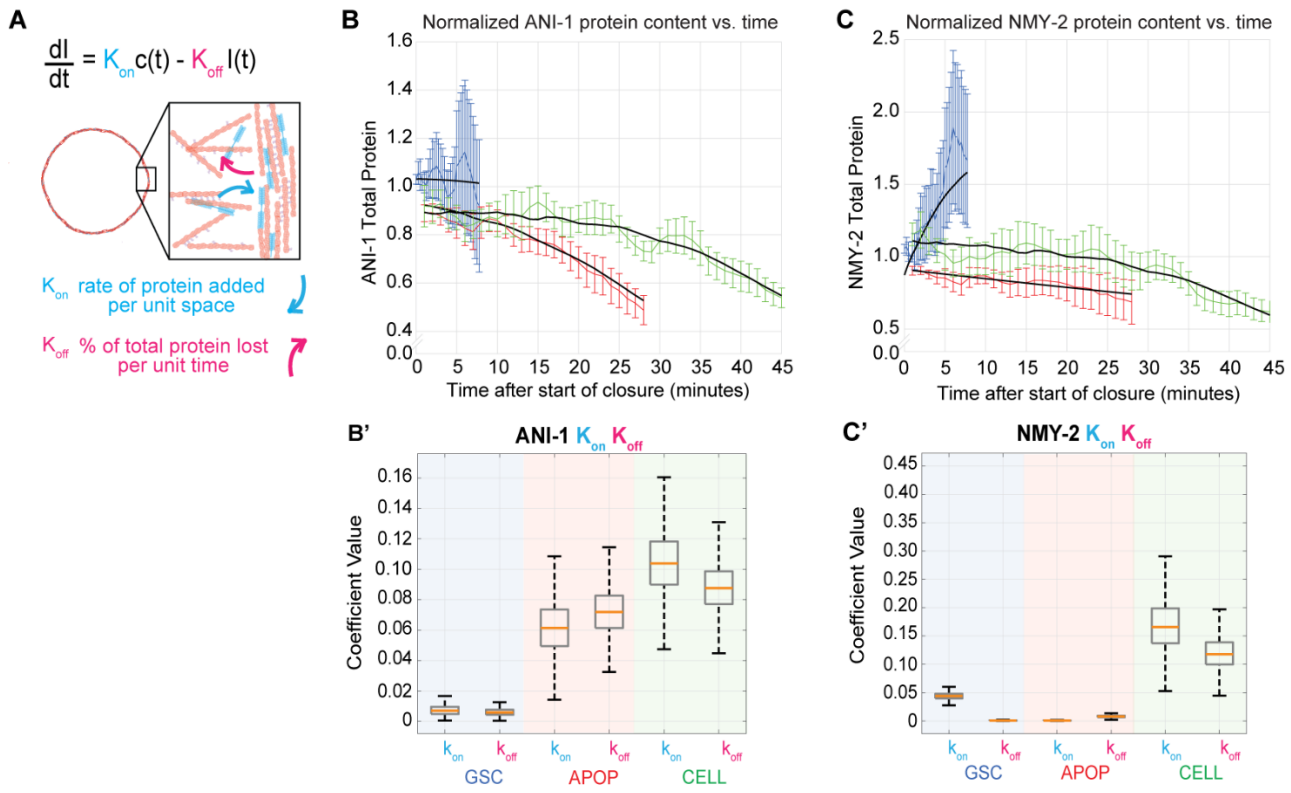

Figure 4: Time-dependent model of ANI-1 and NMY-2 abundance throughout ring closure. Protein content estimates are normalized to initial fluorescence intensity. The mean value of protein fluorescence intensity at each time and standard error is shown. A) Model schematic: the change in the fluorescence intensity, $\frac{dI}{dt}$, in pixels around the circumference of the ring is due to changes in the number of fluorescently labeled molecules within the area of a pixel. In the model, the change in the fluorescence intensity is dependent on a rate of protein flux onto the ring per unit area per unit time, k_{on}, and a parameter k_{off} describing the fraction of the total protein shed from the ring per unit of time. B) GSC cytokinesis (blue), apoptotic cell compartment (red), cellularizing nascent oocyte (green); ANI-1 normalized protein fluorescence intensity population time series, black lines: model prediction generated using the mean value of the distribution of likely values for k_on, k_off. C) NMY-2 normalized protein fluorescence intensity population time-series, GSC (blue), apoptosis (red), cellularization (green), with model predictions generated from the mean value of likely parameter values for k_on, k_off (black). B', C') Coefficient value distributions for k_on, k_off determined using the MCMC method.

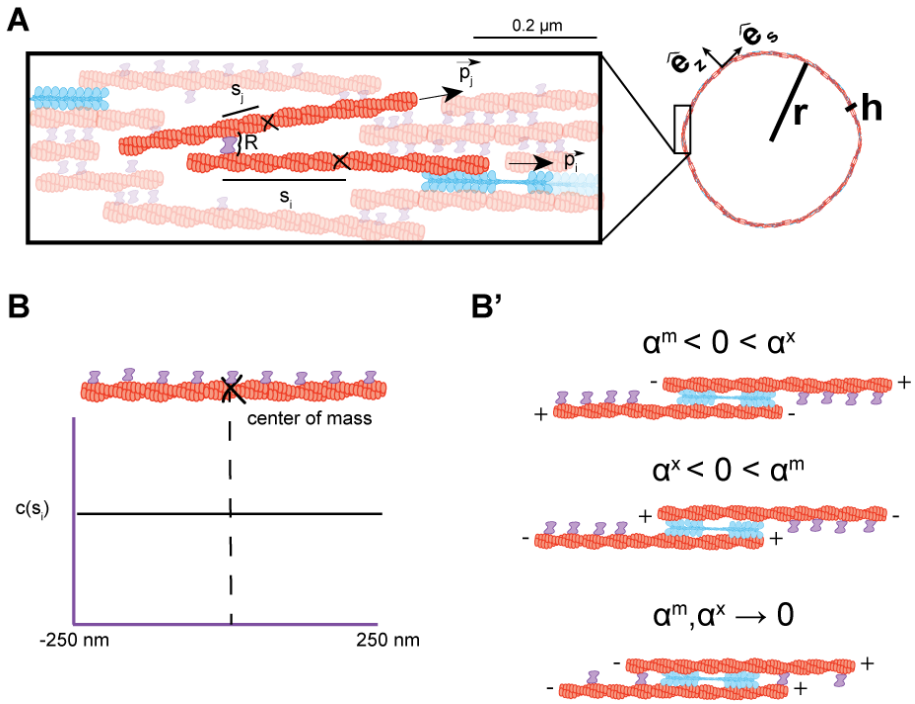

Figure 5) Theory for actomyosin rings. A) An actomyosin ring with radius r and width h is described with the normal unit vector $\hat{e}_z$ and tangent unit vector $\hat{e}_s$. Schematic of forces exerted on filament i by neighbor filaments j through motor or crosslinking head of width 13 nm. The force experienced by filament i depends on the distance of the motor or crosslinker head from the respective filament's center of mass. Each filament has an orientation described by the unit vector $\vec{p}$. B) Schematic of protein distribution along f-actin length when the distribution of protein is uniform. B') Schematic of asymmetrically distributed protein along F-actin and corresponding α.

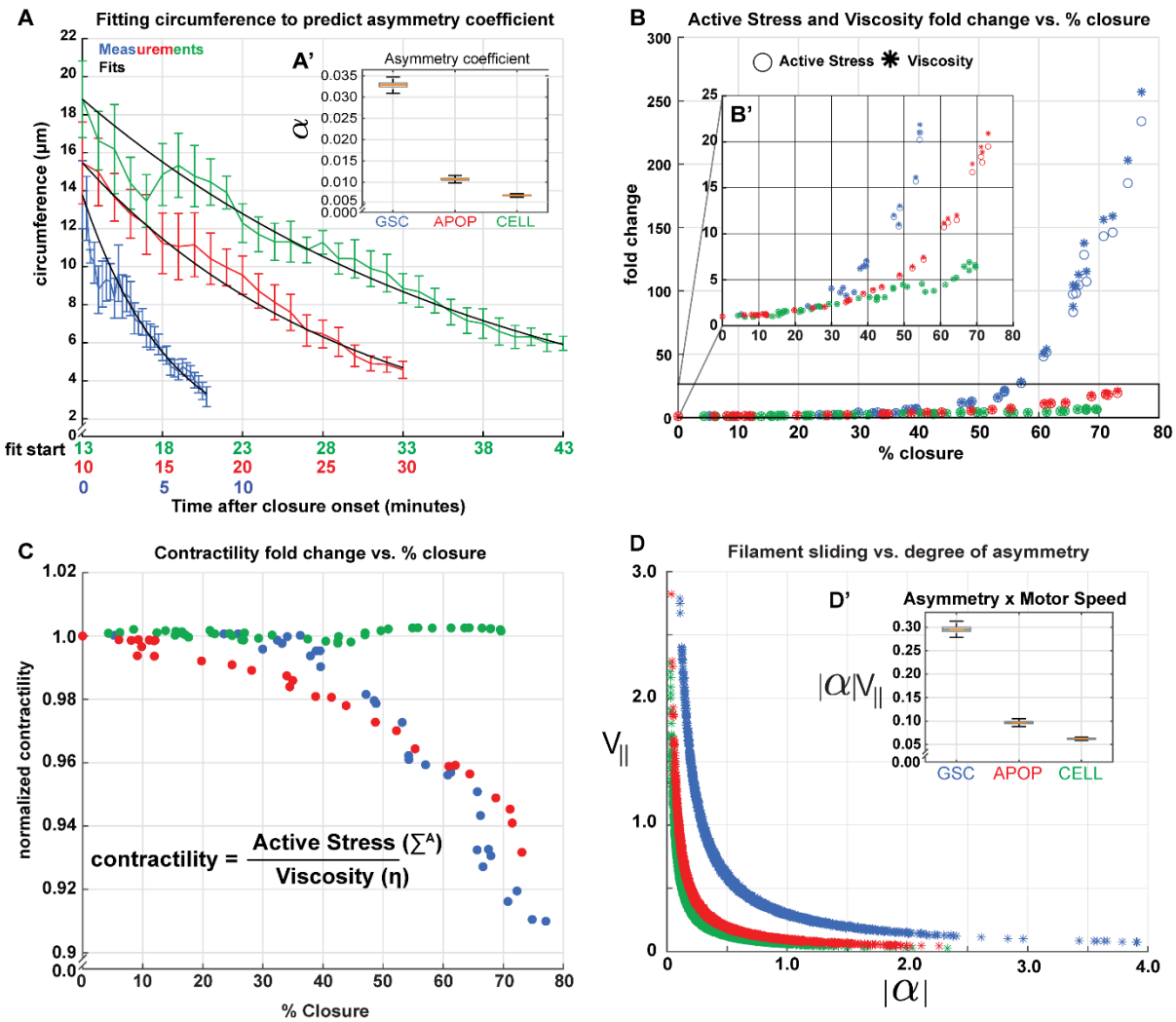

Figure 6: Minimal model and the evolution of ring active stress and viscosity. Actomyosin ring closure curves generated using measured fold changes of ANI-1 and NMY-2. A: Single parameter model; an asymmetry in the distribution of crosslinker along the length of F-actin (condition $c_1^x > 0; c_1^m = 0$). Blue, GSC Cytokinesis; red, apoptosis; green, cellularization. A') Boxplots of asymmetry coefficient value distributions determined by MCMC method. B) Fold change in active stress and viscosity. B') Magnified plot of active stress and viscosity. C) Ring contractility vs. percentage closure. D) NMMII motoring $V_{||}$ is inversely correlated to the asymmetry parameter α, GSC cytokinesis (blue), apoptosis (red), cellularization (green). D') The product of asymmetry parameter α and motor speed $V_{||}$.

References

Bear, JE, and Haugh, JM (2014). Directed migration of mesenchymal cells: where signaling and the cytoskeleton meet. Curr Opin Cell Biol 30, 74–82.

Bourdages, KG, Lacroix, B, Dorn, JF, Descovich, CP, and Maddox, AS (2014). Quantitative analysis of cytokinesis in situ during C. elegans postembryonic development. PLoS ONE 9, e110689.

Burnett, K, Edsinger, E, and Albrecht, DR (2018). Rapid and gentle hydrogel encapsulation of living organisms enables long-term microscopy over multiple hours. Commun Biol 1, 73.

Calvert, MEK, Wright, GD, Leong, FY, Chiam, K-H, Chen, Y, Jedd, G, and Balasubramanian, MK (2011). Myosin concentration underlies cell size-dependent scalability of actomyosin ring constriction. J Cell Biol 195, 799–813.

Capco, DG, and Bement, WM (1991). Analysis of cellular signaling events, the cytoskeleton, and spatial organization of macromolecules during early Xenopus development. Methods Cell Biol 36, 249–270.

Carvalho, A, Desai, A, and Oegema, K (2009). Structural memory in the contractile ring makes the duration of cytokinesis independent of cell size. Cell 137, 926–937.

Cheffings, TH, Burroughs, NJ, and Balasubramanian, MK (2016). Actomyosin ring formation and tension generation in eukaryotic cytokinesis. Curr Biol 26, R719–R737.

Chib, S, and Greenberg, E (1995). Understanding the Metropolis-Hastings Algorithm. The American Statistician 49, 327.

Cortes, DB, Dawes, A, Liu, J, Nickaeen, M, Strychalski, W, and Maddox, AS (2018). Unite to divide - how models and biological experimentation have come together to reveal mechanisms of cytokinesis. J Cell Sci 131.

Cortes, DB, Maddox, PS, Nédéléç, FJ, and Maddox, AS (2022). Contractile ring composition dictates kinetics of in silico contractility. Biophys J.

Courtemanche, N, Pollard, TD, and Chen, Q (2016). Avoiding artefacts when counting polymerized actin in live cells with LifeAct fused to fluorescent proteins. Nat Cell Biol 18, 676–683.

Cuda, G, Pate, E, Cooke, R, and Sellers, JR (1997). In vitro actin filament sliding velocities produced by mixtures of different types of myosin. Biophys J 72, 1767–1779.

D'Avino, PP (2009). How to scaffold the contractile ring for a safe cytokinesis - lessons from Anillin-related proteins. J Cell Sci 122, 1071–1079.

Davies, T, Kim, HX, Romano Spica, N, Lesea-Pringle, BJ, Dumont, J, Shirasu-Hiza, M, and Canman, JC (2018). Cell-intrinsic and -extrinsic mechanisms promote cell-type-specific cytokinetic diversity. ELife 7.

De Lozanne, A, and Spudich, JA (1987). Disruption of the Dictyostelium myosin heavy chain gene by homologous recombination. Science 236, 1086–1091.

Dorn, JF, Zhang, L, Phi, T-T, Lacroix, B, Maddox, PS, Liu, J, and Maddox, AS (2016). A theoretical model of cytokinesis implicates feedback between membrane curvature and cytoskeletal organization in asymmetric cytokinetic furrowing. Mol Biol Cell 27, 1286–1299.

Fang, X, Luo, J, Nishihama, R, Wloka, C, Dravis, C, Travaglia, M, Iwase, M, Vallen, EA, and Bi, E (2010). Biphasic targeting and cleavage furrow ingression directed by the tail of a myosin II. J Cell Biol 191, 1333–1350.

Foster, PJ, Fürthauer, S, and Fakhri, N (2022). Active mechanics of sea star oocytes. BioRxiv.

Fürthauer, S, Lemma, B, Foster, PJ, Ems-McClung, SC, Yu, C-H, Walczak, CE, Dogic, Z, Needleman, DJ, and Shelley, MJ (2019). Self-straining of actively crosslinked microtubule networks. Nat Phys 15, 1295–1300.

Fürthauer, S, Needleman, DJ, and Shelley, MJ (2021). A design framework for actively crosslinked filament networks. New J Phys 23, 013012.

Gartner, A, Boag, PR, and Blackwell, TK (2008). Germline survival and apoptosis. WormBook, 1–20.

Glotzer, M (2005). The molecular requirements for cytokinesis. Science 307, 1735–1739.

Green, RA, Paluch, E, and Oegema, K (2012). Cytokinesis in animal cells. Annu Rev Cell Dev Biol 28, 29–58.

Gumienny, TL, Lambie, E, Hartwieg, E, Horvitz, HR, and Hengartner, MO (1999). Genetic control of programmed cell death in the Caenorhabditis elegans hermaphrodite germline. Development 126, 1011–1022.

Guo, B, and Guilford, WH (2006). Mechanics of actomyosin bonds in different nucleotide states are tuned to muscle contraction. Proc Natl Acad Sci USA 103, 9844–9849.

Haglund, K, Nezis, IP, and Stenmark, H (2011). Structure and functions of stable intercellular bridges formed by incomplete cytokinesis during development. Commun Integr Biol 4, 1–9.

Hall, DH, Winfrey, VP, Blaeuer, G, Hoffman, LH, Furuta, T, Rose, KL, Hobert, O, and Greenstein, D (1999). Ultrastructural features of the adult hermaphrodite gonad of Caenorhabditis elegans: relations between the germ line and soma. Dev Biol 212, 101–123.

Hirsh, D, Oppenheim, D, and Klass, M (1976). Development of the reproductive system of Caenorhabditis elegans. Dev Biol 49, 200–219.

Hoffman, MD, and Gelman, A (2011). The No-U-Turn Sampler: Adaptively Setting Path Lengths in Hamiltonian Monte Carlo. ArXiv.

Kadzik, RS, Homa, KE, and Kovar, DR (2020). F-Actin Cytoskeleton Network Self-Organization Through Competition and Cooperation. Annu Rev Cell Dev Biol 36, 35–60.

Kamasaki, T, Osumi, M, and Mabuchi, I (2007). Three-dimensional arrangement of F-actin in the contractile ring of fission yeast. J Cell Biol 178, 765–771.

Khaliullin, RN, Green, RA, Shi, LZ, Gomez-Cavazos, JS, Berns, MW, Desai, A, and Oegema, K (2018). A positive-feedback-based mechanism for constriction rate acceleration during cytokinesis in Caenorhabditis elegans. ELife 7.

Kitayama, C, Sugimoto, A, and Yamamoto, M (1997). Type II myosin heavy chain encoded by the myo2 gene composes the contractile ring during cytokinesis in Schizosaccharomyces pombe. J Cell Biol 137, 1309–1319.

Koch, EA, and King, RC (1969). Further studies on the ring canal system of the ovarian cystocytes of Drosophila melanogaster. Z Zellforsch Mikrosk Anat 102, 129–152.

Kučera, O, Siahaan, V, Janda, D, Dijkstra, SH, Pilátová, E, Zatecka, E, Diez, S, Braun, M, and Lansky, Z (2021). Anillin propels myosin-independent constriction of actin rings. Nat Commun 12, 4595.

Kumar, V, and Elkouby, YM (2023). Tools to analyze the organization and formation of the germline cyst in zebrafish oogenesis. Development 150.

Lan, H et al. (2019). An extracellular matrix protein promotes anillin-dependent processes in the Caenorhabditis elegans germline. Life Sci Alliance 2.

Lee, K-Y, Green, RA, Gutierrez, E, Gomez-Cavazos, JS, Kolotuev, I, Wang, S, Desai, A, Groisman, A, and Oegema, K (2018). CYK-4 functions independently of its centralspindlin partner ZEN-4 to cellularize oocytes in germline syncytia. ELife 7.

Li, D et al. (2015). ADVANCED IMAGING. Extended-resolution structured illumination imaging of endocytic and cytoskeletal dynamics. Science 349, aab3500.

Lord, M, Laves, E, and Pollard, TD (2005). Cytokinesis depends on the motor domains of myosin-II in fission yeast but not in budding yeast. Mol Biol Cell 16, 5346–5355.

Ma, X, Kovács, M, Conti, MA, Wang, A, Zhang, Y, Sellers, JR, and Adelstein, RS (2012). Nonmuscle myosin II exerts tension but does not translocate actin in vertebrate cytokinesis. Proc Natl Acad Sci USA 109, 4509–4514.

Mabuchi, I, and Okuno, M (1977). The effect of myosin antibody on the division of starfish blastomeres. J Cell Biol 74, 251–263.

Maddox, AS, Habermann, B, Desai, A, and Oegema, K (2005). Distinct roles for two C. elegans anillins in the gonad and early embryo. Development 132, 2837–2848.

Mahajan-Miklos, S, and Cooley, L (1994). Intercellular cytoplasm transport during Drosophila oogenesis. Dev Biol 165, 336–351.

Mangione, MC, and Gould, KL (2019). Molecular form and function of the cytokinetic ring. J Cell Sci 132.

Martin, AC (2020). The physical mechanisms of drosophila gastrulation: mesoderm and endoderm invagination. Genetics 214, 543–560.

McCarter, J, Bartlett, B, Dang, T, and Schedl, T (1999). On the control of oocyte meiotic maturation and ovulation in Caenorhabditis elegans. Dev Biol 205, 111–128.

Mendes Pinto, I, Rubinstein, B, Kucharavy, A, Unruh, JR, and Li, R (2012). Actin depolymerization drives actomyosin ring contraction during budding yeast cytokinesis. Dev Cell 22, 1247–1260.

Miura, K (2020). Bleach correction ImageJ plugin for compensating the photobleaching of time-lapse sequences. F1000Res 9, 1494.

Nagy, A, Takagi, Y, Billington, N, Sun, SA, Hong, DKT, Homsher, E, Wang, A, and Sellers, JR (2013). Kinetic characterization of nonmuscle myosin IIb at the single molecule level. J Biol Chem 288, 709–722.

Neal, RM (1993). Probabilistic inference using Markov chain Monte Carlo methods, Department of Computer Science, University of Toronto.

Nguyen, LT, Swulius, MT, Aich, S, Mishra, M, and Jensen, GJ (2018). Coarse-grained simulations of actomyosin rings point to a nodeless model involving both unipolar and bipolar myosins. Mol Biol Cell 29, 1318–1331.

Niederman, R, and Pollard, TD (1975). Human platelet myosin. II. In vitro assembly and structure of myosin filaments. J Cell Biol 67, 72–92.

O'Shaughnessy, B, and Thiyagarajan, S (2018). Mechanisms of contractile ring tension production and constriction. Biophys Rev 10, 1667–1681.

Okada, H, MacTaggart, B, Ohya, Y, and Bi, E (2021). The kinetic landscape and interplay of protein networks in cytokinesis. IScience 24, 101917.

Osório, DS, Chan, F-Y, Saramago, J, Leite, J, Silva, AM, Sobral, AF, Gassmann, R, and Carvalho, AX (2019). Crosslinking activity of non-muscle myosin II is not sufficient for embryonic cytokinesis in C. elegans. Development 146.

Ozugergin, I, Mastronardi, K, Law, C, and Piekny, A (2022). Diverse mechanisms regulate contractile ring assembly for cytokinesis in the two-cell Caenorhabditis elegans embryo. J Cell Sci 135.

Ozugergin, I, and Piekny, A (2022). Diversity is the spice of life: An overview of how cytokinesis regulation varies with cell type. Front Cell Dev Biol 10, 1007614.

Palani, S et al. (2017). Motor Activity Dependent and Independent Functions of Myosin II Contribute to Actomyosin Ring Assembly and Contraction in Schizosaccharomyces pombe. Curr Biol 27, 751–757.

Patil, A, Huard, D, and Fonnesbeck, CJ (2010). PyMC: Bayesian Stochastic Modelling in Python. J Stat Softw 35, 1–81.

Pepling, ME, and Spradling, AC (1998). Female mouse germ cells form synchronously dividing cysts. Development 125, 3323–3328.

Piekny, AJ, and Maddox, AS (2010). The myriad roles of Anillin during cytokinesis. Semin Cell Dev Biol 21, 881–891.

Pollard, TD, and Wu, J-Q (2010). Understanding cytokinesis: lessons from fission yeast. Nat Rev Mol Cell Biol 11, 149–155.

Pollard, TD (2014). The value of mechanistic biophysical information for systems-level understanding of complex biological processes such as cytokinesis. Biophys J 107, 2499–2507.

Pollard, TD (2017). Nine unanswered questions about cytokinesis. J Cell Biol 216, 3007–3016.

Povea-Cabello, S et al. (2017). Dynamic Reorganization of the Cytoskeleton during Apoptosis: The Two Coffins Hypothesis. Int J Mol Sci 18.

Rehain-Bell, K, Love, A, Werner, ME, MacLeod, I, Yates, JR, and Maddox, AS (2017). A Sterile 20 Family Kinase and Its Co-factor CCM-3 Regulate Contractile Ring Proteins on Germline Intercellular Bridges. Curr Biol 27, 860–867.

Sain, A, Inamdar, MM, and Jülicher, F (2015). Dynamic force balances and cell shape changes during cytokinesis. Phys Rev Lett 114, 048102.

Schindelin, J et al. (2012). Fiji: an open-source platform for biological-image analysis. Nat Methods 9, 676–682.

Schwayer, C, Sikora, M, Slováková, J, Kardos, R, and Heisenberg, C-P (2016). Actin rings of power. Dev Cell 37, 493–506.

Sinard, JH, Stafford, WF, and Pollard, TD (1989). The mechanism of assembly of Acanthamoeba myosin-II minifilaments: minifilaments assemble by three successive dimerization steps. J Cell Biol 109, 1537–1547.

Stam, S, Alberts, J, Gardel, ML, and Munro, E (2015). Isoforms confer characteristic force generation and mechanosensation by myosin II filaments. Biophys J 108, 1997–2006.

Straight, AF, Cheung, A, Limouze, J, Chen, I, Westwood, NJ, Sellers, JR, and Mitchison, TJ (2003). Dissecting temporal and spatial control of cytokinesis with a myosin II Inhibitor. Science 299, 1743–1747.

Swulius, MT, Nguyen, LT, Ladinsky, MS, Ortega, DR, Aich, S, Mishra, M, and Jensen, GJ (2018). Structure of the fission yeast actomyosin ring during constriction. Proc Natl Acad Sci USA 115, E1455–E1464.

Turlier, H, Audoly, B, Prost, J, and Joanny, J-F (2014). Furrow constriction in animal cell cytokinesis. Biophys J 106, 114–123.

Vavylonis, D, Wu, J-Q, Hao, S, O'Shaughnessy, B, and Pollard, TD (2008). Assembly mechanism of the contractile ring for cytokinesis by fission yeast. Science 319, 97–100.

Wang, K, Okada, H, and Bi, E (2020). Comparative Analysis of the Roles of Non-muscle Myosin-IIs in Cytokinesis in Budding Yeast, Fission Yeast, and Mammalian Cells. Front Cell Dev Biol 8, 593400.

Weeds, AG, and Lowey, S (1971). Substructure of the myosin molecule. II. The light chains of myosin. J Mol Biol 61, 701–725.

Winkelman, JD, Suarez, C, Hocky, GM, Harker, AJ, Morganthaler, AN, Christensen, JR, Voth, GA, Bartles, JR, and Kovar, DR (2016). Fascin- and α-Actinin-Bundled Networks Contain Intrinsic Structural Features that Drive Protein Sorting. Curr Biol 26, 2697–2706.

Wloka, C, and Bi, E (2012). Mechanisms of cytokinesis in budding yeast. Cytoskeleton (Hoboken) 69, 710–726.

Wu, J-Q, and Pollard, TD (2005). Counting cytokinesis proteins globally and locally in fission yeast. Science 310, 310–314.

Zhang, L, and Maddox, AS (2010). Anillin. Curr Biol 20, R135-6.

Zumdieck, A, Kruse, K, Bringmann, H, Hyman, AA, and Jülicher, F (2007). Stress generation and filament turnover during actin ring constriction. PLoS ONE 2, e696.